nature communications

Article

https://doi.org/10.1038/s41467-025-62518-y

Operando neutron imaging-guided gradient design of Li-ion solid conductor for high-mass-loading cathodes

Received: 31 May 2024

Accepted: 22 July 2025

Published online: 18 August 2025

Check for updates

Tongtai Ji[1], Yuxuan Zhang[2], James Torres[2], Aleksandar S. Mijailovic[3], Ya Tang[4,5], Xianhui Zhao[4], Jean-Christophe Bilheux[2], Jiwei Wang[1], Brian W. Sheldon[3], Oluwafemi Oyedeji[4] & Hongli Zhu[1]

High-mass-loading cathodes are crucial for achieving high energy density in all-solid-state batteries from the lab scale to industry. However, as mass-loading increases, electrochemical performance is significantly compromised due to sluggish kinetics. In this work, *operando* neutron imaging is deployed on a high-mass-loading NMC 811 cathode of 33 mg/cm^2 (5.0 mAh/cm^2) and directly visualizes the lithiation prioritization of the cathode active material (CAM) from the solid electrolyte membrane side to the current collector side. In addition to the tortuosity, another key limitation on ion transfer in the cathode arises from the mismatch between the uniform distribution of the solid electrolyte (catholyte) in the conventional composite cathode and the non-uniform Li^+ flux generated by the faradaic reaction of CAMs. Therefore, we engineer a gradient in the catholyte concentration to match the Li^+ flux distribution as a means of eliminating the ion transfer obstacle. This approach demonstrates enhanced rate performance, even with high-mass-loading cathodes. A $LiCoO_2$ composite cathode with 100 mg/cm^2 high-mass-loading exhibits an areal capacity of 10.4 mAh/cm^2 at a current density of 2.25 mA/cm^2. This work provides insight into the ion-transport limitation in thick cathodes and demonstrates an effective gradient design to overcome the kinetic barrier and achieve high battery performance.

All-solid-state batteries (ASSBs) are among the most promising next-generation energy storage technologies. These batteries offer the potential for high energy density and significantly enhanced safety by replacing flammable organic liquid electrolytes (LEs) with non-flammable inorganic solid electrolytes (SEs)[1]. To improve their energy density, many researchers have focused on developing electrode materials with high specific capacity or high potential. However, the cell-level energy density is much lower than that of the material level because of the substantial content of inactive materials, such as the battery case, current collectors, solid electrolytes, and other components that do not directly contribute to capacity. Therefore, increasing the mass-loading of the cathode is considered to be one of the most effective strategies for achieving the proposed high energy density at the cell level[2].

Achieving excellent electrochemical performance in high-mass-loading cathodes is significantly more challenging than in thin cathodes. In the thick electrode, the higher areal current density under the same C-rate leads to a much larger ohmic polarization across the entire cell, and the increased tortuosity and longer diffusion paths result in sluggish ionic and electronic transport kinetics[3–5].

[1]Department of Mechanical and Industrial Engineering, Northeastern University, Boston, MA, USA. [2]Neutron Scattering Division, Oak Ridge National Laboratory, Oak Ridge, TN, USA. [3]School of Engineering, Brown University, Providence, RI, USA. [4]Oak Ridge National Laboratory, Oak Ridge, TN, USA. [5]Thayer School of Engineering, Dartmouth College, Hanover, NH, USA. e-mail: h.zhu@neu.edu

The specific mechanism of the decay of the rate performance in thick electrodes is more complicated, especially for ion transfer. In LEs, the transport of Li^+ is based on the combination of electric-field-induced migration and salt concentration gradient-induced diffusion[6]. Under a high rate, a large Li salt concentration gradient in the liquid phase will be formed and further hinder the Li^+ diffusion, and the Li^+ depletion in the LE will cause the underutilization of the cathode active materials (CAMs)[7,8]. However, for the inorganic SE used in ASSBs, anions are fixed, and Li^+ is the only ion that can move with a Li^+ transference number around 1.0. Thus, there is no Li^+ gradient or concertation change in SEs. Moreover, an increasing number of SEs demonstrate high ionic conductivities, sometimes surpassing those of LEs[9–12]. Therefore, ASSBs are supposed to have improved rate capabilities[13]. Although impressive rate performance (>40 C) has been achieved in ASSBs, the cathode mass-loading is usually low (<5 mg/cm^2)[14,15]. The rate performances of high-mass-loading cathode ASSBs still fall short of expectations.

In the composite cathode of ASSBs, the Li^+ ion transfer paths are formed solely by the solid–solid contact between the CAM and SE particles. Compared to LE-based batteries, thick cathodes in ASSBs exhibit much higher tortuosity and lower effective ionic conductivity[16,17]. The size, proportion, and arrangement of the CAM, SE, and electron-conductive additive particles must be optimized carefully[18]. Inspired by the LE-based batteries, a low-ionic-tortuosity design has been introduced to the ASSBs by mixing different sizes of SE particles to improve the rate performance[19]. Nevertheless, despite the absence of Li^+ concentration gradients in SEs, recent studies have observed non-uniform reactions of CAMs in ASSBs[20,21]. Given the unique physical properties of SEs compared to LEs, the impact of these properties on the performance of thick electrodes in ASSBs remains unclear. Therefore, it is crucial to investigate kinetic transfer in high-mass-loading cathodes using direct *operando* visualization techniques and provide insights for designing thick cathodes with uniform and fast ion transport in all-solid-state systems.

Operando and in-situ investigation with sufficient temporal and spatial resolution is important in understanding the kinetics of the thick cathode (>100 µm) in ASSBs, especially by tracking the Li behavior and reaction uniformity on the electrode level. Conventional characterization methods, such as electron-beam and optical-light-based methods, are not well suited for detecting electrochemical reactions in CAMs[22]. X-ray-based methods also have difficulty detecting Li directly due to its low X-ray attenuation coefficient[23]. X-ray diffraction (XRD) and X-ray absorption spectroscopy (XAS) are powerful tools for detecting the state of charge (SoC) evolution of CAMs[24,25], but these spectroscopy-based data often lack the ability to provide operando visualization with a large characterization area. In contrast, neutron imaging has unique advantages for tracking Li transport because of Li's high visibility in both ionic and metallic states[22,23,26–28]. In addition, neutron imaging has great Li isotope contrast, so it can be used to track Li^+ diffusion in the solid electrolyte[29]. Thus, neutron imaging is a powerful *operando* characterization method for ASSBs.

Herein, to identify the limit factor of the electrochemical reaction in thick cathodes in ASSBs, *operando* neutron imaging was successfully conducted to visualize the reaction gradient over the whole thick cathode with a mass-loading of 33 mg/cm^2 (~180 µm thick). By performing image calculation, the spatial inhomogeneous reaction of CAMs was observed. Image analysis combined with electrochemical analysis identified the mismatch between the non-uniform Li^+ flux and the homogeneous SE distribution in the thick cathode as the main cause of poor electrochemical performance. Based on the visualized electrochemical reaction gradient within the thick cathode, we strategically designed a three-layer cathode with a catholyte content gradient to promote fast Li^+ transport and uniform reaction throughout the entire thick cathode. By tailoring the catholyte content to match the Li^+ flux at different depths within the cathode, this design aims to alleviate the kinetic limitations observed in high-mass-loading ASSB cathodes, which could ultimately lead to enhanced electrochemical rate performance. As a result, high-mass-loading cathodes—100 mg/cm^2 with theoretical areal capacities of 15.0 mAh/cm^2 for $LiNi_{0.8}Co_{0.1}Mn_{0.1}O_2$ (NMC 811) and 11.25 mAh/cm^2 for $LiCoO_2$ (LCO)—based on a three-layer design, showed significantly improved rate performances compared to that of the thick cathode without SE gradient and given the same CAMs content.

Results and discussion

Visualizing reaction kinetics in high-mass-loading cathodes through operando neutron imaging

Low-mass-loading cathodes (<5 mg/cm^2 or 1.0 mAh/cm^2) are commonly employed in research to investigate material-level capabilities and usually demonstrate excellent rate performance. However, as cathode mass-loading increases, poor kinetics become a significant issue. Ion transfer, electron transfer, interface resistance, ion diffusion, and electron transfer in the CAM are the most common factors that contribute to kinetic limitations in composite cathodes (Fig. 1a). The ion and electron transfer will further affect the reaction prioritization and uniformity of CAMs on the electrode level. Despite results in previous work that have demonstrated thick and high areal capacity cathodes (>10 mAh/cm^2), this capacity was obtained at a low rate (0.025 C), even when utilizing a highly ion-conductive SE with a conductivity of 32 mS/cm[9]. Faster cycling of high-mass-loading cathodes in ASSBs without compromising rate performance is crucial for real-world applications. However, the primary bottleneck for achieving high-mass-loading cathodes in ASSBs remains unclear, so efforts to investigate cathode mass-loading are essential.

To investigate the limitation on reaction kinetics, *operando* neutron imaging was carried out to visualize the reaction homogeneity within a thick cathode during charge and discharge processes (Supplementary Fig. 1). Figure 1b illustrates the mechanism and setup of *operando* neutron imaging for ASSBs. The *operando* cell, featuring a high-mass-loading cathode (33 mg/cm^2 and 5.0 mAh/cm^2), was positioned vertically in front of the detector, and the layer interfaces were aligned parallel to the neutron beam. Given the distinct neutron attenuation coefficients of the materials in the ASSB (Supplementary Table 1), the intensity of the transmitted neutron beam varies after passing through the battery. This variance facilitates easy differentiation between the cathode, SE, and anode layers based on the gray level; differentiation can be achieved by normalizing the neutron transmission intensity (Tr) from zero (no transmission) to one (full transmission). Darker areas correspond to lower neutron transmission, indicating that the material has a higher neutron attenuation coefficient. In the neutron image, the three layers—the In–^{6}Li anode, SE, and the thick cathode—could be clearly recognized from top to bottom (Fig. 1b). Subsequently, the battery underwent charging and discharging processes while simultaneously collecting electrochemical impedance spectroscopy (EIS) data (Supplementary Fig. 2) and *operando* neutron imaging data. Note that some variations could affect the performance of the *operando* cell during beamline operation. These factors are discussed in Supplementary Discussion 1 (Supplementary Fig. 3).

To amplify changes in the cell's neutron transmission during charge and discharge, the *operando* images were further processed by dividing each image at a given time point by the image taken at the pristine state to obtain the transmission change ratio, Tr_t/Tr_0 (Fig. 1c). Pseudo-color was applied to represent the value of Tr_t/Tr_0 in the neutron image (Fig. 1d–f). For the area with limited transmission change ($Tr_t/Tr_0 \approx 1$), the color remains green. Color shifts toward red and blue indicate a decrease ($Tr_t/Tr_0 < 1$) and increase ($Tr_t/Tr_0 > 1$) of the neutron transmission, respectively. Supplementary Movie 1 shows a pseudo-color video that depicts the transmission change over the charge and discharge process. The cylindrical shape of the *operando* cell results in different neutron beam transmission lengths over the

https://doi.org/10.1038/s41467-025-62518-y

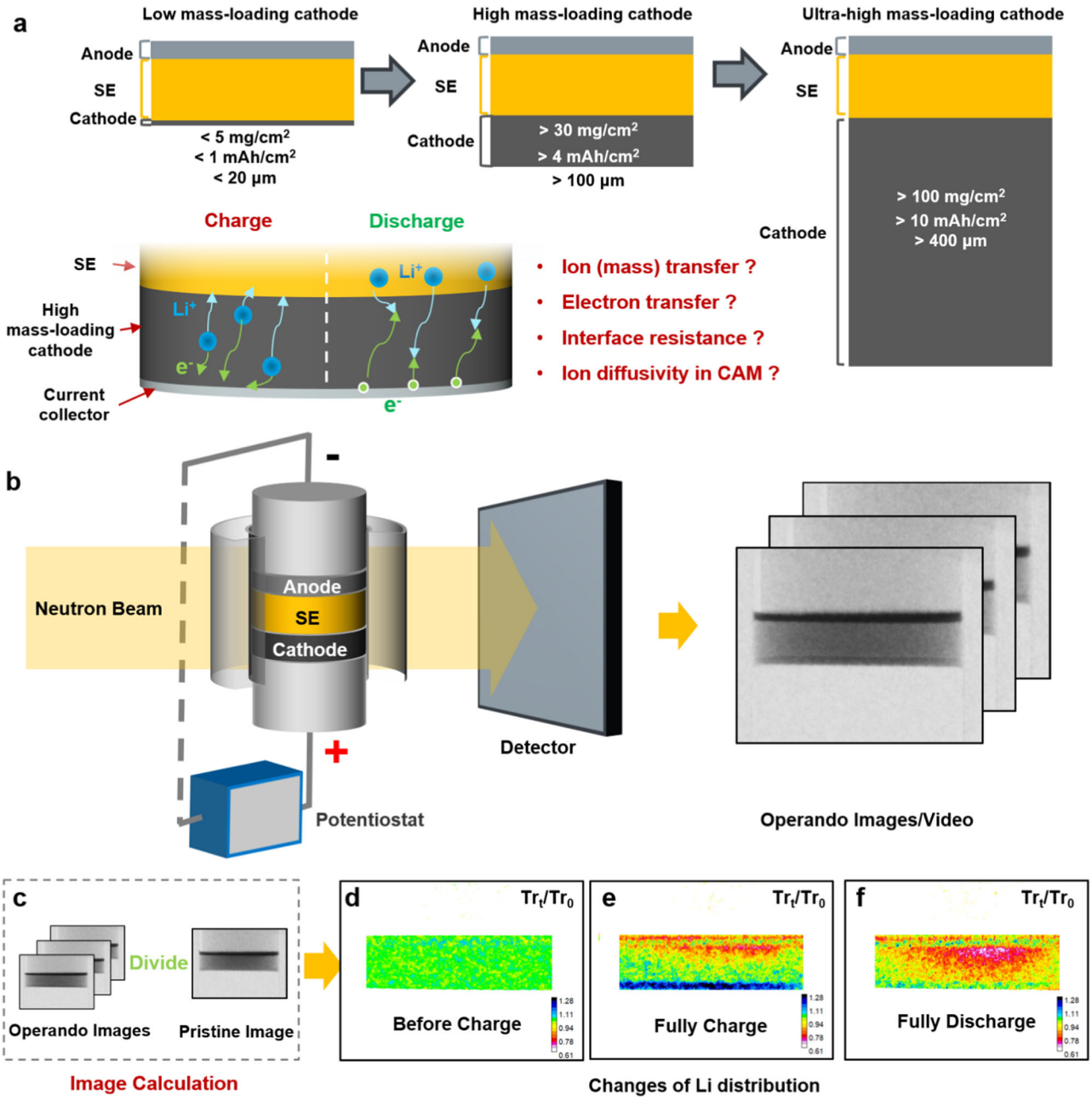

Fig. 1 | Schematics of different mass-loading cathodes in ASSBs and the setup of *operando* neutron imaging. a Configurations with different mass-loadings and the influence factors for the kinetic issues in the thick cathode. **b** Schematic of the experimental setup of *operando* neutron imaging. **c** Schematic of the image calculation process. The results at different states: **d** before charge, **e** fully charged, and **f** fully discharged, presented by the pseudo-color images. Source data are provided as a Source Data file.

cross-section and further affects the neutron transmission. Therefore, to obtain the most reliable data (Supplementary Fig. 4), we narrowed the sampling region to the center area (1.2 mm) of the cell such that the transmission length was close to the cell diameter (4 mm).

To better track the transmission changes over time, the average transmission change ratio of the sampling region of the *operando* battery is plotted in Fig. 2a as a function of time with the corresponding charge/discharge profile. Figures 2b, c provide detailed 2D images at specific SoCs and depths of discharge (DoDs). We focused on the behaviors at the whole-cell level. During the charging process, the colors of the cathode layer gradually changed to blue because the CAM underwent a delithiation process, which resulted in a decrease in the neutron attenuation coefficient (Supplementary Table 1). The Li^+ flux was directed toward the anode side during charging, but there was almost no transmission change in the SE layer with a thickness of around 700 μm; this result proves that there was no Li^+ concentration change in the SE layer, since Li^+ in both CAM and SE is natural Li. A small amount of red color was observed at the interface between the SE and the In–^{6}Li anode, caused by the self-diffusion of $^6Li^+$ from the anode layer to the SE layer by replacing the natural Li^+ in SE[30]. For the In–^{6}Li anode layer, due to the high neutron attenuation coefficients of In and ^{6}Li, the neutron transmission remained at almost zero throughout the process under the current setup, resulting in no observable transmission change.

During the discharge process, the Li^+ flux was directed toward the cathode side. As the CAMs underwent lithiation, the color of the cathode layer gradually turned from blue back to green after discharge. For the SE layer, based on the data from the charging process,

https://doi.org/10.1038/s41467-025-62518-y

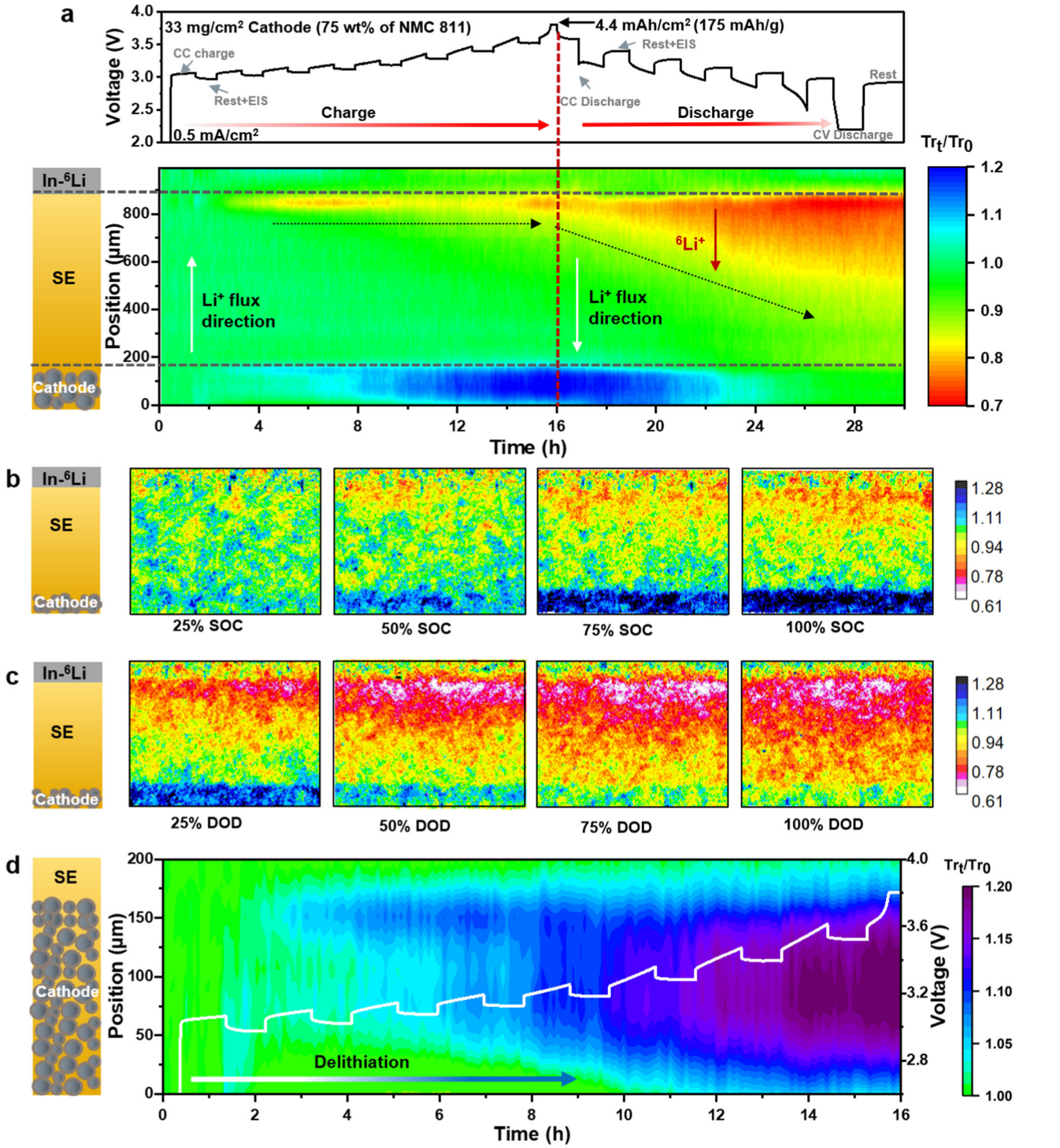

Fig. 2 | *Operando* neutron imaging of the thick cathode in ASSBs. a The average neutron transmission change ratio (Tr_t/Tr_0) of the *operando* neutron imaging cell as a function of time and the corresponding charge/discharge curve. Pseudo color 2D images of the *operando* cell at different **b** state of charge (SoC) and **c** depth of discharge (DoD); **d** Zoomed-in neutron transmission change (Tr_t/Tr_0) for the thick cathode layer during the charging process with the corresponding voltage profile. Source data is provided as a Source Data file. The negative electrode is In–Li. The stack pressure is 50 MPa at a temperature of 15 to 20 °C.

Li^+ flux did not affect the Li^+ concentration and neutron attenuation coefficient of the SE layer. Therefore, in Fig. 2a, the enlargement of the red color region in SE during discharge was contributed by $^6Li^+$ diffusing into the SE, along with the Li^+ flux. Because $^6Li^+$ replaced the natural Li^+ in the SE, the SE's neutron attenuation coefficient significantly increased (Supplementary Table 1). A clear front of $^6Li^+$ proceeding through the SE from the anode side to the cathode side was observed, which can also be seen in Fig. 2c as well as Supplementary Movie 1. The *operando* neutron imaging successfully visualized the Li^+ diffusion in ASSBs from the anode to the cathode side through the SE layer during discharge, using the ^6Li isotope to enhance neutron contrast.

The cathode layer was further magnified with enhanced contrast to investigate the delithiation uniformity of the CAM along the vertical direction (Fig. 2d). The thickness of the composite cathode layer with a mass-loading of 33 mg/cm² (5.0 mAh/cm²) is around 180 μm. At the

start of the discharge, it was difficult to observe the transmission change because of the limited concentration change. After 3 h, with a capacity of around 0.4 mAh/cm^2, the region close to the SE side started to turn blue. As mentioned above, this indicates the delithiation of the CAM. The cathode close to the current collector remained unchanged. As the charging time increased, a gradual movement of the reaction associated with the CAM delithiation was observed, progressing from the SE side toward the current collector side. After around 16 h, the entire cathode turned blue, and a specific charge capacity of 175 mAh/g with a voltage reaching 3.7 V (4.3 V vs Li/Li$^+$) was observed. Note that the cell was charging for one hour and then rested for the EIS within the next hour. We observed that color change and gradient formation occurred mainly during the charging process. During rests, the delithiation gradient was slightly reduced (red circles in Supplementary Fig. 5). One hour of rest is not enough to let the SoC of the CAM become uniform in the whole cathode, and the rest does not affect the direction of the delithiation gradient that we identified above. A corresponding simulation by Newman pseudo two-dimensional (P2D) model was then carried out as shown in Supplementary Fig. 6 to test our observation. The simulation result is well aligned with our *operando* neutron image data, showing that changes in delithiation gradients are minor during the rest stages. (Note that the simulations described herein are intended to capture general trends, but have not been calibrated for precise quantitative predictions). A similar trend was also observed for the discharge process (Supplementary Fig. 7). The CAM close to the SE side first turned back to green, indicating that the lithiation process also started from the SE side.

A relatively thinner cathode (16.7 mg/cm^2) was also characterized using *operando* neutron imaging (Supplementary Fig. 8). The reaction inhomogeneity is not obvious in the thin cathode (Supplementary Fig. 9). Although both the thick and thin cathode cells were cycled under the same C-rate, the thin cathode cell shows small overpotential because of the smaller areal current density. Moreover, the color change in the SE layer due to the ^{6}Li$^+$ diffusion in the discharge process was much lighter in the thin cathode, reflecting the smaller Li$^+$ flux and corresponding with the smaller current density.

Identifying the key factors limiting ion transport in thick cathodes

The reaction uniformity of the thick electrode is closely linked to the reaction kinetics, especially the transport of charge carriers (both for ions and electrons). In early studies of the composite cathode used in ASSBs, electron-conductive additives (mainly carbon) were usually avoided in the composite cathode because of concerns about SE decomposition upon contact with high-surface-area carbon[31,32]. The electron conductive pathway only relies on the contact between CAM particles. Therefore, the restriction of electron transport increases with increasing SE content because of the contact loss between CAM particles[17]. However, one-dimensional vapor-grown carbon fibers have proven to be ideal electron-conductive additives in ASSBs due to their excellent electrical conductivity. SE decomposition is significantly reduced in the composite cathode when using one-dimensional carbon fibers as the electron-conductive additive[33]. Based on our cycling test result (Supplementary Fig. 10), there is almost no capacity decay. Therefore, electron-conductive additives were applied in our composite cathode. Our *operando* neutron imaging data reveal that the delithiation and lithiation processes of CAM were nonuniform in the thick cathode. Most of the Li$^+$ ions first reacted in the area near the SE layer and experienced difficulty reaching the CAM close to the current collector; this finding indicates that the electrochemical reaction kinetics were primarily restricted by Li$^+$ ion transport along the long pathway within the thick electrode, rather than by electron transfer.

To further diagnose the ion transport limitation within the thick cathode, electrochemical performances were examined with cathode mass-loadings of 3, 10, and 30 mg/cm^2 at 60 °C. Indium–lithium symmetric cells were also studied to evaluate the In–Li anode behavior and determine whether the anode contributes to the battery performance limitations. The symmetric cells maintained stable performance with limited overpotential (<100 mV), even at high current densities of up to 15.0 mA/cm^2 (Supplementary Figs. 11 and 12). This result proved that the anode is not the main performance barrier in our ASSBs system. To explore the intrinsic rate performance on the material level of NMC 811 with minimal influence from electrode thickness, a low-mass-loading (3 mg/cm^2) cathode with high SE content (33.0 wt%) and sufficient carbon additives (2.0 wt% of carbon nanofibers) was tested. The cell shows a specific discharge capacity of 199 mAh/g at C/10, approaching the theoretical capacity of NMC 811 (Fig. 3a). At C/2, 1 C, and 2 C, the capacities were 174, 160, and 141 mAh/g, respectively, representing the rate capacity of our NMC 811 at the material level under conditions designed to minimize ion and electron transport limitations at the electrode level.

We further evaluated the rate performance for our normal cathode (75.0 wt% NMC with 1.5 wt% of carbon nanofibers) with mass-loadings of 10 and 30 mg/cm^2. When using a mass-loading of 10 mg/cm^2 with an areal capacity of 1.5 mAh/cm^2, there is no obvious decay of the rate performance: discharge capacities of 194, 170, 153, and 134 mAh/g were observed at C/10, C/2, 1 C, and 2 C, respectively (Fig. 3b). However, when the mass-loading was increased to 30 mg/cm^2 with an areal capacity of 4.5 mAh/cm^2, the rate performance significantly decreased. The discharge capacities were 152, 140, 109, 80, and 49 mAh/g at C/10, C/2, 1 C, and 2 C, respectively (Fig. 3c), which represent only 76%, 63%, 50%, and 35%, respectively, of the corresponding values achieved in the 3 mg/cm^2 cell. The great rate performance of the 10 mg/cm^2 cathode was due to the short ion pathway within the thin electrodes, whereas the cell with a 30 mg/cm^2 cathode showed a significantly poorer rate performance, suggesting an insufficient reaction of the cathode materials within the thick electrode because of sluggish ion transport along the long ion pathway.

The reaction homogeneity at the electrode level can also be characterized by the dQ/dV analysis[34]. For the CAM (NMC 811), the intrinsic dQ/dV curve has four clear peaks representing the sequential intercalation reactions of NMC 811[35]. As shown in Fig. 3d, the dQ/dV curve for the 3 mg/cm^2 cathode at the low rate (C/10) corresponds to the standard behavior of the CAM at the material level. The four peaks can be observed even at 1C. When the rate increases to 2C, the shape of the dQ/dV curve changes to a rounded rectangle. Since the cathode is very thin, this behavior mainly contributes to the rate capacity of CAM on the material level. In other words, it is due to the lithiation gradient on the particle level. We conducted simulations of the SoC variation of the CAM under different rates with the Newman P2D model for the very thin cathode (3 mg/cm^2) to explain this phenomenon, as shown in Supplementary Fig. 13. For the very thin cathode, the lithiation inhomogeneity comes mainly from the particle level rather than the electrode level. For increased mass-loading (10 and 30 mg/cm^2), both through-thickness and intra-particle lithiation gradients were observed (Supplementary Fig. 14).

Using the dQ/dV curves of the 3 mg/cm^2 cathode as the baseline, we further analyzed the effects of the increase in mass-loading. For the cathodes with 10 and 30 mg/cm^2 mass-loadings (Fig. 3e, f), both cells show four pairs of peaks indicating uniform and sequential multiphase transitions under a low rate of C/10 or C/20. With the increase in the rate, the change of the dQ/dV curves of the 10 mg/cm^2 mass-loading cathode is similar to our baseline. However, for the cathode with 30 mg/cm^2 mass-loading, the trend of the dQ/dV curves varies with the increase of the C-rate. Even at C/10, four pairs of peaks are difficult to observe. At C/5, there is a peak emerging at 3.4 V (Fig. 3f), which is a peak but not a shift of peak two because it cannot be simply corrected by the IR drop[34]. The shape of the dQ/dV curve for oxidation transforms into a semi-isosceles triangle (yellow line in Fig. 3f). When the rate increases to C/2, the shape of the dQ/dV curve

https://doi.org/10.1038/s41467-025-62518-y

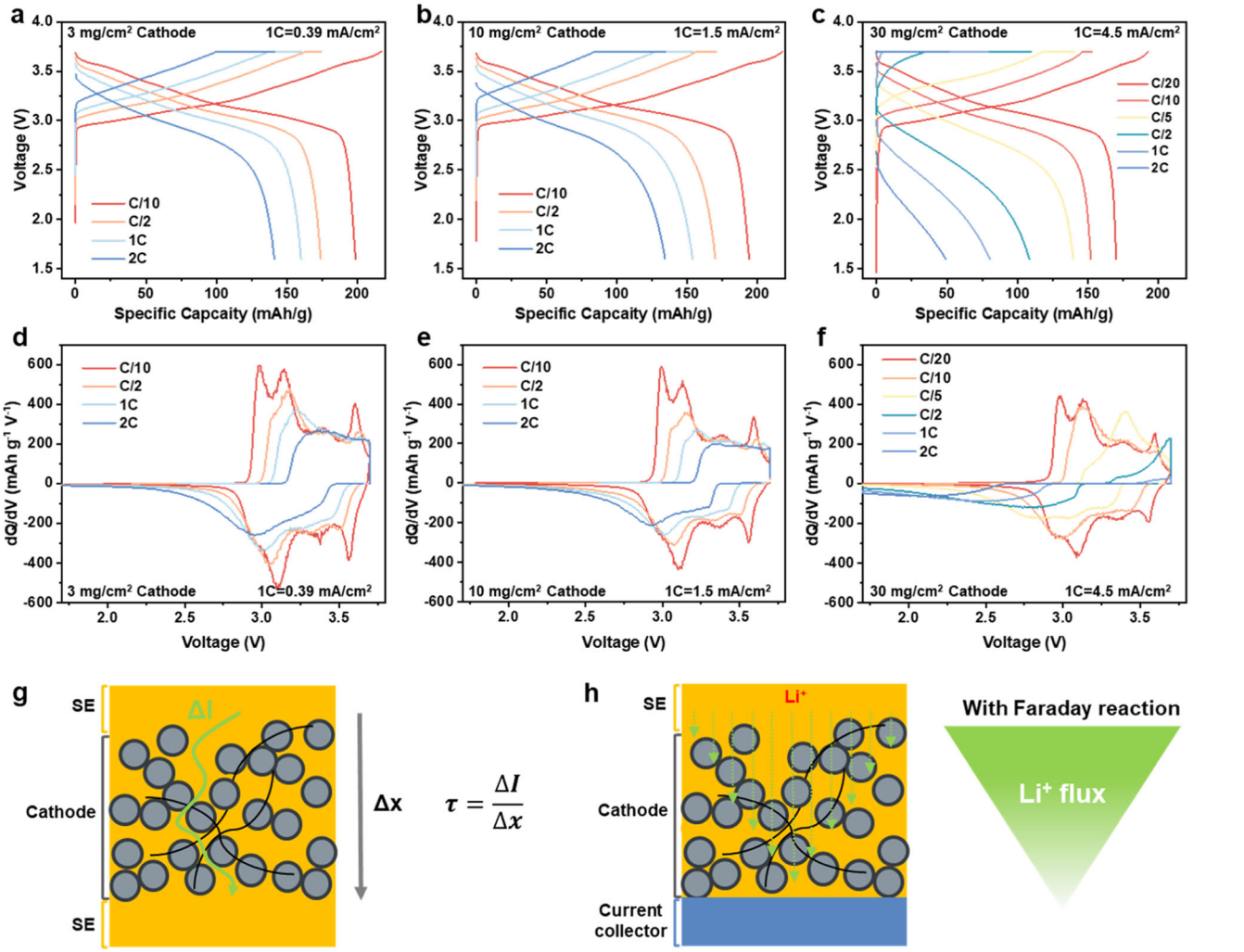

Fig. 3 | Electrochemical investigation of the ASSBs with different mass-loading cathodes. Charge and discharge profiles of the ASSBs with different mass-loading cathodes of **a** 3 mg/cm², **b** 10 mg/cm², and **c** 30 mg/cm²; and the corresponding d*Q*/d*V* curves of the ASSBs with different mass-loading cathodes of **d** 3 mg/cm², **e** 10 mg/cm², and **f** 30 mg/cm². **g** Schematic of the setup for measuring the effective ion conductivity of the composite cathode with the electron block electrode and the geometric definition of tortuosity. **h** Schematic of the Li^+ flux distribution crossing the thick cathode with faradaic reaction during charge and discharge. Source data are provided as a Source Data file. The negative electrode is In–Li. The stack pressure is 50 MPa at a temperature of 60 °C.

of the thick cathode becomes a right triangle (blue line in Fig. 3f), which is significantly different from that of the thin cathode of 3 and 10 mg/cm². The sequential intercalation reactions of NMC 811 were completely unobservable. Although the lithiation inhomogeneity that happened on both particle level and electrode level can affect the d*Q*/d*V* curve, the different behavior of the 30 mg/cm² when compared with the 3 mg/cm² and 10 mg/cm² cathodes indicates that the huge inhomogeneity at the electrode level is the key reason for the obvious change of the d*Q*/d*V* curves of the thick cathode. The simulation results of local particle surface SoC and particle average SoC as a function of position for electrodes with different mass loadings (Supplementary Fig. 14) also clearly demonstrated that SoC variation on the electrode level is much more severe than the SoC variation on the particle level for the thick cathode (30 mg/cm²), which is distinctive with the phenomenon of the thin cathodes (both 3 and 10 mg/cm²). The strange d*Q*/d*V* curves indicate the huge reaction inhomogeneity in the thick cathode of 30 mg/cm², especially at high rates, and these trends correspond well with the simulated d*Q*/d*V* curves (Supplementary Figs. 15 and 16), which is consistent with the findings from the *operando* neutron imaging.

While the electrochemical results and *operando* neutron imaging provide valuable insights into the reaction inhomogeneity and performance limitations in thick cathodes, it is essential to understand the underlying factors that contribute to these issues. In much of the literature, ionic tortuosity (τ) and effective ion conductivity are considered key parameters in the kinetics of the cathode in terms of controlling Li^+ diffusion and transportation in the electrodes[21,36]. Tortuosity is defined as the ratio of the actual path length through a structure (Δl) to the straight-line distance between the starting and end points of that pathway (Δx) (Fig. 3g)[18]. In order to reduce the tortuosity, many researchers focus on building continuous ion transport pathways and low-tortuosity structural designs in ASSBs and have found great success[5]. Nevertheless, in the thick cathode, we should note that the distribution of Li^+ flux on the whole-electrode level will be dramatically different on the current collector side compared with the SE side because of the accumulation of Li^+ flux generated by the faradaic reaction of the CAM with increasing thickness, as shown in Fig. 3h. In terms of the Li^+ flux distribution, the ion transfer paths requirement varies among the whole electrodes. To adapt the Li^+ flux gradient, a gradient SE content design of the thick cathode in ASSBs was inspired by the gradient porosity design in LE-based batteries[37–39]. In contrast with LEs, there is no Li^+ concentration variation in the SE with a transference number of 1, which avoids the occurrence of electrolyte depletion in the thick cathode of LE-based batteries. In addition, the

https://doi.org/10.1038/s41467-025-62518-y

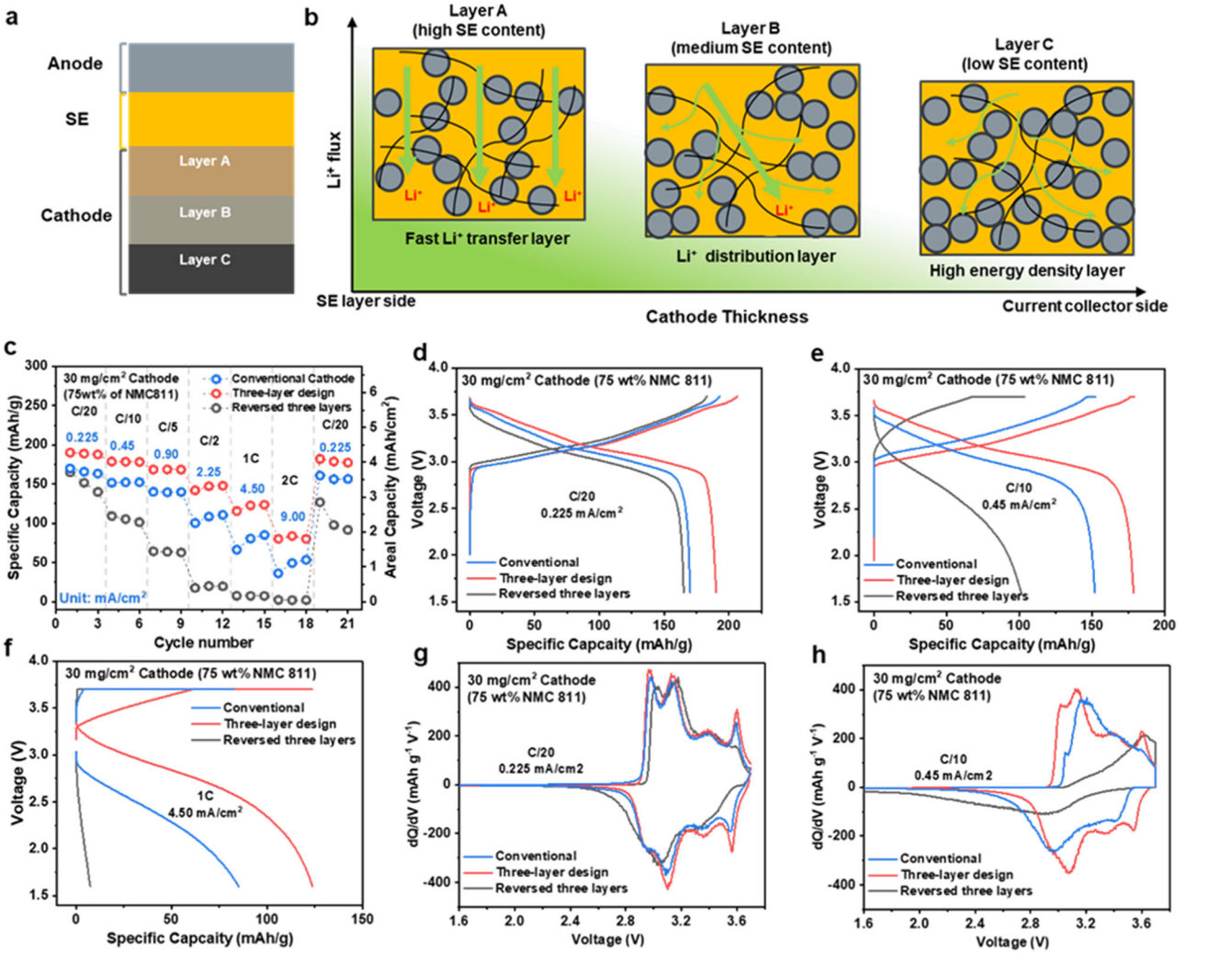

Fig. 4 | Schematic and evaluation of the three-layer cathode with gradient design. a Schematic of the three-layer cathode with gradient design and **b** the design details of each layer corresponding to the Li^+ flux over the thickness of the cathode. **c** Comparison of the capacities at different rates for the three-layer cathode, reversed three-layer cathode, and the control group without the gradient design. The comparison of charge and discharge curves at **d** C/20, **e** C/10, and **f** 1 C, and the dQ/dV curves at **g** C/20 and **h** C/10. Source data are provided as a Source Data file. The negative electrode is In–Li. The stack pressure is 50 MPa at a temperature of 60 °C.

following equation relates concentration gradients and potential gradients to the current in the electrolyte phase:

$$i_l = -\kappa_{eff}\nabla\phi_l + \left(\frac{2\kappa_{eff}RT(1-t_+)}{F}\right)\left(1+\frac{d\ln f_{\pm}}{d\ln c}\right)\nabla\ln c., \qquad (1)$$

where i_l is the current in the electrolyte phase, κ_{eff} is the effective ionic conductivity, ϕ_l is the potential in the electrolyte, t_+ is the transference number, F is Faraday's constant, $\frac{d\ln f_{\pm}}{d\ln c}$ is the activity, and c is the electrolyte concentration. A transference number of 1 results in the omission of the second term, which reduces potential gradients in the LE and therefore reaction inhomogeneity[40]. The absence of concentration gradients in SEs allows for more precise control over ion transport pathways to match the Li^+ flux distribution at the electrode level. Therefore, appropriate allocation of SE gradient with Li^+ flux over the thick cathode could effectively improve the rate performance.

Gradient design in high-mass-loading cathode for enhancing rate performance

Based on the findings from the *operando* neutron imaging and the above-mentioned point of Li^+ flux generated from the faradaic reaction, we designed a three-layer cathode with gradient ion transport paths for realizing homogenous electrochemical reaction and improved rate performance in the thick cathode by adjusting the SE content with the Li^+ flux distribution (Fig. 4a, b). The overall CAM content in the three-layer cathode was kept at 75.0 wt%, which is the same as the non-gradient thick cathode. From the SE layer side to the current collector side, layer A is the fastest Li^+ transfer layer, with 65.0 wt% CAM, 33.0 wt% SE, and 2.0 wt% carbon nanofibers. The highest SE content is designed to bear the largest Li^+ flux close to the SE layer. More carbon additives were also used to prevent electron isolation of the CAM due to the high SE content. Layer B is composed of 75.0 wt% CAM, 23.5 wt% SE, and 1.5 wt% carbon nanofibers, the same as the original composite cathode. Layer C is a high-energy-density layer with the highest CAM content (85.0 wt.%) and lowest SE content (14.0 wt.%). A comparison group with a reversed sequence of the three layers was also prepared, as well as a control group with only one composition of 75.0 wt% CAM, 23.5 wt% SE, and 1.5 wt% carbon nanofibers.

The rate capabilities of the three different cathodes were compared to evaluate the effectiveness of our gradient design (Fig. 4c). The results show that the rate performance of the cell with the three-layer cathode outperforms that of the cell without a gradient design, even when tested under a very low current rate of C/20. The superiority of

the gradient cathode is further exaggerated when the current rate increased from C/20 to high rates of C/10, C/5, C/2, 1 C, and 2 C (9.0 mA/cm^2), with 112%, 119%, 120%, 135%, 155%, and 171% of the capacities obtained from the conventional cathode, respectively. To further verify that the designed gradient ion transport paths can benefit the rate performance for the thick cathode, a reversed gradient cathode was examined, and it shows a much worse rate performance than that of the non-gradient cathode. Although the initial discharge capacity of the reversed three-layer cathode is very close to the original single-layer cathode at the low rate (C/20), its capacity decays dramatically as the rate increases. There is almost no capacity obtained when the rate is higher than C/2.

We further compared the charge/discharge profiles of these three groups to dig into the fundamentals of the three-layer design. Under the lowest rate we tested (C/20) with a current density of 0.225 mA/cm^2 (Fig. 4d), the three-layer cathode exhibited a noticeably smaller overpotential and larger capacity. As the C-rate increased, the advantage became more pronounced (Fig. 4e, f). The dQ/dV analysis can provide more detailed insights into kinetics. As shown in Fig. 4g, at C/20 the dQ/dV curves of the three-layer cathode and the conventional cathode are very similar, with four pairs of peaks corresponding to the sequential intercalation reactions of NMC 811. However, for the reversed three-layer cathode, in addition to the shift of the peaks due to the larger overpotential, one pair of peaks at high voltage (around 3.6 V vs. In–Li/Li$^+$ or 4.2 V vs Li/Li$^+$) is missing due to the sluggish kinetics. Specifically, the low SE content of the top layer creates significant resistance for the Li$^+$ transfer into or out of the cathode, resulting in a rapid voltage rise to the cut-off voltage without the last phase transition ($H_2 \rightarrow H_3$) of NMC 811. When the rate increases to C/10 (Fig. 4h), the cell with the three-layer cathode still clearly shows the four pairs of peaks for the sequential intercalation reactions, indicating a homogeneity reaction throughout the cathode thickness. However, for the conventional and reversed cathodes, the four pairs of peaks become blurred, wider, or even disappear as a result of reaction inhomogeneity at the electrode level during the charge and discharge process[34]. Overall, the three-layer cathode demonstrates better rate performance with more homogenous delithiation and lithiation reactions across the entire cathode. Although the three-layer cathode and reversed groups have the same tortuosity, they show dramatically different performances. We conducted simulations with the Newman P2D model to study the three-layer design's effect on the SoC uniformity. In supplementary Fig. 17, the local SoC vs. position is shown for the NMC811 monolayer, three-layer, and reversed three-layer designs for a C/2 charge with 30 mg/cm^2 mass-loading. The distribution of the SoC shows increased SoC near the separator for the three-layer design and decreased SoC near the separator for the reversed three-layer design, compared to the monolayer. These results provide evidence that the appropriate allocation of SE content to match the Li$^+$ flux over the whole thick cathode is an effective way to improve homogeneous electrochemical reactions and the rate performance of the thick cathode.

To further explore the performance of our three-layer design cathode, we introduced another CAM, $LiCoO_2$ (LCO). LCO shows much better C-rate performance on the material level (Supplementary Fig. 18). In the dQ/dV curves for the low-mass-loading (3 mg/cm^2) LCO cell, there is almost no shift of the reaction peaks, even when the rate increases to 2 C (Supplementary Fig. 19). Therefore, the LCO cathode can better exhibit the ion transfer improvement on the electrode level. The thick LCO cathode (30 mg/cm^2) with the three-layer design shows almost no capacity decay even when the rate increases to 2.5 C (8.44 mA/cm^2), with an areal capacity of over 3.0 mAh/cm^2 (Fig. 5a, b). In contrast, a dramatic decay in rate performance was observed for the ASSB with the reversed three-layer LCO cathode (Fig. 5c). Because there is no rate limitation at the material level and the interface between SE and CAM is identical, the remarkable difference between two cells primarily relies on the different ion transport kinetics at the electrode level, which further highlights the significance of aligning the arrangement of the SE content with Li$^+$ flux to the ion transport in the thick cathode.

High-mass-loading cathodes (100 mg/cm^2) with theoretical capacities of 15.0 and 11.25 mAh/cm^2 for NMC 811 and with LCO as the CAM were also studied (Fig. 5d-i). The high-mass-loading NMC 811 cathode with the three-layer design exhibited around 189 and 170 mAh/g specific capacity for the first charge and discharge, which is equivalent to 14.25 and 12.75 mAh/cm^2 areal capacity under a current density of 0.38 mA/cm^2. Even under current densities of 1.5 and 3.0 mA/cm^2, the cell can still obtain the capacities of 9.9 and 7.9 mAh/cm^2, which are 1.5 and 2.5 times better, respectively, than the conventional cell. The high-mass-loading LCO cathode with the three-layer design exhibited even better rate performance, achieving an areal capacity of 10.4 mAh/cm^2 at a current density of 2.25 mA/cm^2. All of them show obvious improvement in rate performance compared with the traditional one-layer cathode, further corroborating the importance of aligning the SE arrangement with the Li$^+$ flux on the thick electrode.

With an increase in current density over 10 mA/cm^2 for the 30 mg/cm^2 cathode and over 5 mA/cm^2 for the 100 mg/cm^2 cathode, all cells met an abnormal failure (Supplementary Figs. 20 and 21). The capacity suddenly decreases within a few cycles. For example, the cell with a 30 mg/cm^2 LCO cathode cycled stably at 2.5C with a current density of 8.44 mA/cm^2 (Supplementary Fig. 22). However, when the current increased to 10.13 mA/cm^2, the overpotential suddenly increased even over the cutoff voltage. The constant current (CC) charge period disappeared, and the capacity was obtained by the constant voltage (CV) charge process. This phenomenon cannot be simply explained as the ohmic resistance because it is not linearly related to the current density when compared with the increase in overpotential from 2C (6.75 mA/cm^2) to 2.5C (8.44 mA/cm^2) (Supplementary Fig. 23). The abnormal failure is also not due to the rate performance of the CAM since both materials experienced the same issue under a similar current density. Therefore, the issue is still related to the ion transfer in the thick cathode, and there should be a critical current density for the thick cathode based on the SE content and distribution. Because the Li$^+$ flux gradually increased with the thickness, but our cells provide only a three-level gradient, some mismatches of SE component and Li$^+$ flux still occur on the smaller scale. A smoother and more fine-tuned arrangement of the SE will further increase the critical current density and benefit the rate performance of the thick cathode.

In summary, this work successfully visualized the lithium reaction gradients in an ASSB with a high-mass-loading (33 mg/cm^2) NMC811 cathode using *operando* neutron imaging. The results confirmed the inhomogeneous lithiation of CAM in the thick cathode, with a lithiation gradient from the SE layer side to the current collector side. The electrochemical evaluations of the ASSBs with different cathode mass-loadings of 3, 10, and 30 mg/cm^2 further validated the inhomogeneous lithiation of CAM in the thick cathode, especially at high rates. Based on the study, ion transfer was identified as the key limitation causing kinetic issues in the thick cathode. We pioneered the concept of "Li$^+$ flux" and its effect on ion transfer in the thick cathode of ASSBs. Due to the Faradaic reactions of the cathode active materials (CAMs), which consume or generate Li$^+$ ions, the Li$^+$ flux across the ion conductor (mainly the catholyte) accumulates proportionally with the cathode thickness. The mismatch between the Li$^+$ flux and ion transfer paths creates a huge obstacle for the Li$^+$ transport in the thick cathode.

To address the ion transfer limitation arising from the significant variation in Li$^+$ flux from the SE layer to the current collector side in the thick cathode, a tailored arrangement of the catholyte in the composite cathodes was designed and studied. This setup resulted in significantly improved rate performances: 171% of the capacity obtained in the conventional cathode at a current density of 9.0 mA/cm^2 for a 30 mg/cm^2 NMC 811 cathode. The effectiveness of this gradient design

https://doi.org/10.1038/s41467-025-62518-y

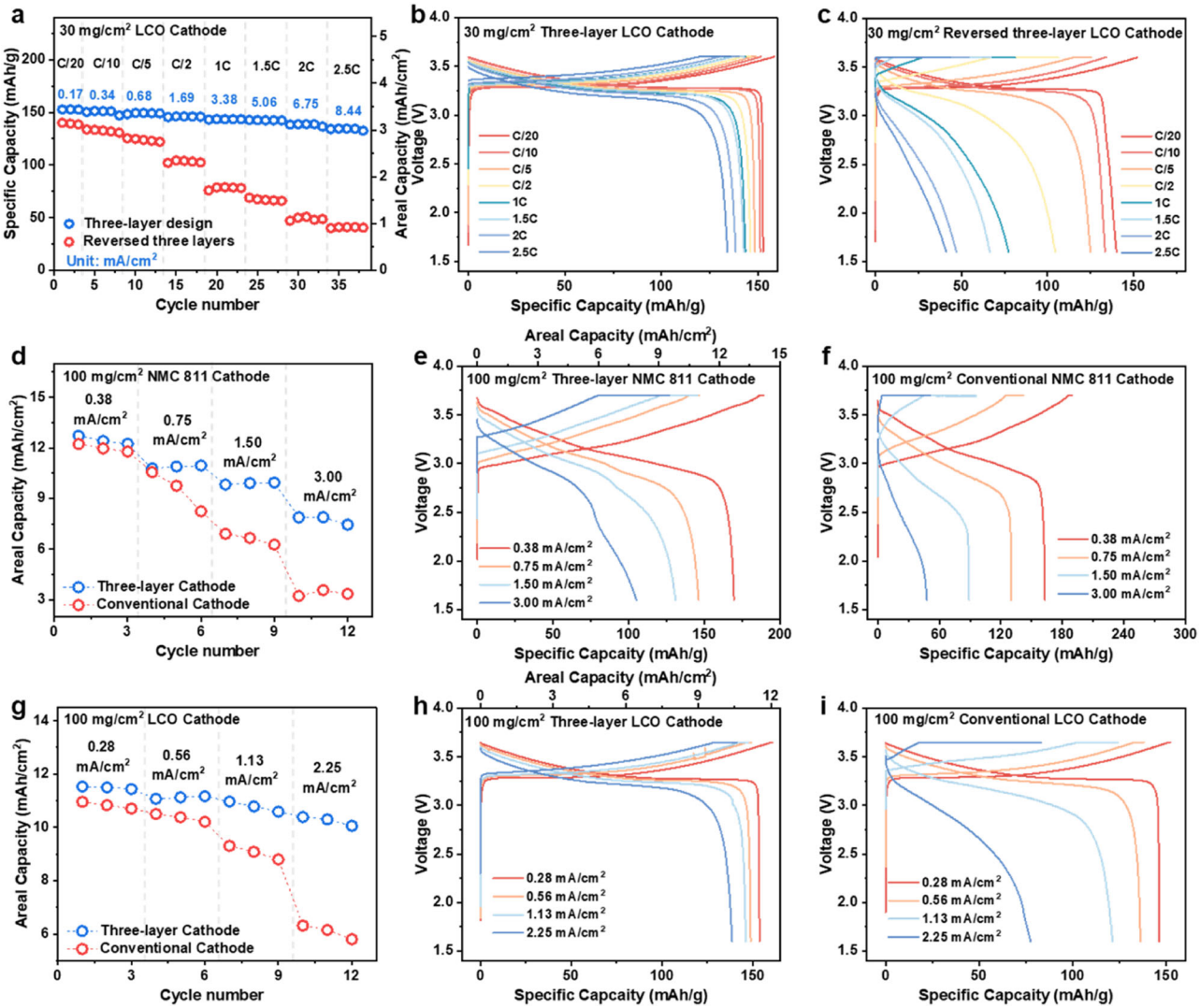

Fig. 5 | Electrochemical performances of the high-mass-loading cathodes with the three-layer gradient design. Comparison of the rate performances of ASSBs: **a** 30 mg/cm² high-mass-loading LCO cathode with three-layer design and reversed three-layer cathode, and the specific charge/discharge profiles of **b** the three-layer cathode and **c** the reversed three-layer cathode. **d** Comparison of the rate performances of ASSBs with the three-layer cathode and conventional one-layer cathode with 100 mg/cm² high-mass-loading NMC 811 cathode, and the charge/discharge profiles of batteries with **e** the three-layer cathode and **f** conventional one-layer cathode. **g** Comparison of the rate performances of ASSBs with three-layer cathode and traditional one-layer cathode with a 100 mg/cm² high-mass-loading LCO cathode, and the charge/discharge profiles of batteries with **h** three-layer cathode and **i** conventional one-layer cathode. Source data are provided as a Source Data file. The negative electrode is In–Li. The stack pressure is 50 MPa at a temperature of 60 °C.

was further demonstrated in high-mass-loading cathodes (100 mg/cm²), which achieved areal capacities of 10.4 mAh/cm² at a current density of 2.25 mA/cm² with an LCO cathode and 9.9 mAh/cm² at a current density of 1.50 mA/cm² for an NMC cathode. We also observed a critical current density threshold in the thick electrodes, beyond which an abnormal capacity drop occurs as a result of the mismatch between the catholyte and Li^+ flux at smaller length scales. This work highlights the importance of understanding and optimizing ion transport in high-mass-loading cathodes for the development of high-performance ASSBs. The insights gained from *operando* neutron imaging and the demonstrated effectiveness of the gradient design provide valuable inspiration for future advancements in high-mass-loading, fast-charging ASSB technology.

Methods

Materials preparation

SE, $Li_{5.4}PS_{4.4}Cl_{1.6}$, was prepared by high-energy ball milling with an annealing process[41]. Li_2S (Sigma-Aldrich, 99.98%), P_2S_5 (Sigma-Aldrich, 99%), and LiCl (Sigma-Aldrich, 99%) were stoichiometrically mixed by ball milling for 10 h at 500 rpm. After that, the mixture was annealed at 510 °C for 2 h. The CAMs, single-crystal NMC 811 (Nanoramic Inc., USA) and lithium cobalt oxide (Sigma-Aldrich, 99.8%), were coated with Li_2SiO_x through a wet chemical method to stabilize their interface between the SE[42]. Graphitized carbon nanofibers (US Research Nanomaterials Inc., 99.9%) were used as the electronic conductive additive. The composite cathodes with different CAM weight percentages (65%, 75%, and 85%) were prepared by mixing Li_2SiO_x coated CAMs, SE, and carbon additive. The composite cathodes with different CAM weight percentages (65%, 75%, and 85%) were prepared by mixing Li_2SiO_x-coated CAMs, SE, and carbon additive (65%, 33%, 2% for 65% CAM cathode; 75%, 23.5%, 1.5% for 75% CAM cathode; 85%, 14%, 1% for 85% CAM cathode) by hand milling gently for 30 mins.

Operando Neutron imaging

The *operando* neutron imaging was taken on the Multimodal Advanced Radiography Station (MARS), High Flux Isotope Reactor (HFIR)

beamline CG-1D, at Oak Ridge National Laboratory. The detector-to-pinhole distance was 6.59 m. The pinhole diameter was 11 mm. The cells used for *operando* neutron imaging were assembled in the argon-filled glovebox. Fifteen milligrams (15 mg) of SE was prepressed by 50 MPa within the quartz tube with a diameter of 4 mm. Then, the cathode powder was cast onto one side of the SE pallet with a pressure of 300 MPa. One piece of In (15 mg, Sigma, 99.99%) and one piece of ^{6}Li metal (0.2 mg, Cambridge Isotope Laboratories, Inc., 95%) were sequentially attached to the other side of the SE pallet. An aluminum pillar and a stainless-steel pillar were used as the current collector for the cathode side and anode side, respectively. A stacking pressure of 50 MPa was applied to the cell by an aluminum framework. All gaps on the cell were further sealed by sealing grease and hot melt glue. The battery was operated by a VMP3 potentiostat (BioLogic) with in situ EIS measurement with an AC amplitude of 10 mV from 7 MHz to 10 mHz. Ten (10) points were collected per decade. Before the EIS test, the cell was rested to reach a quasi-stationary potential with a dV/dT <1 mV/min. The open-circuit voltage (OCV) drift correction function was applied during the EIS measurement. For the *operando* neutron imaging collecting, the cell was placed in front of a scientific complementary metal-oxide-semiconductor (sCMOS) camera system (Zyla5.5, Andor Technology plc., Belfast, UK) with a 20 μm thick Gd_2O_2S: Tb scintillator screen. The exposure time for each image was 5 minutes under the neutron beam with a wavelength range of 0.8 to 6 Å and a peak flux of 2.2×10^6 n cm^{-2} s^{-1} at 2.6 Å. The pixel size of the operando neutron image is 7.5 * 7.5 μm. Open beam and dark field images were collected before and after the *operando* neutron imaging test. The ambient temperature was around 20 °C. The neutron imaging Jupyter Notebook developed by ORNL and Fiji-image software were used for the data processing of the *operando* neutron images.

All-solid-state batteries assembly and electrochemical tests

The ASSBs were assembled by the cold pressing method in an argon-filled glovebox. First, 100 mg/cm^2 of SE was pre-pressed into the homemade PEEK cell with a diameter of 1/2 inch (12.7 mm) under 50 MPa. Different amounts of cathode materials were further cast on one side of the SE pellet. For the multi-layer cathode, the cathode materials were cast layer by layer with a pre-press pressure of 10 MPa. The cathode and SE were further densified under a pressure of 300 MPa by two steel pillars. One piece of In foil and Li foil each were sequentially attached to the other side of the SE pellet. An aluminum foil and a copper foil were used as the current collectors for the cathode and anode, respectively. A stacking pressure of 50 MPa was applied to the cell by a stainless-steel framework during cycling. For the battery test at 60 °C, all batteries were placed in the gravity convection oven (Fisher scientific) and cycled by a battery cycler system (LAND Electronic Co., Ltd), with a cut of voltage of 1.6 to 3.7 V for the NMC cathode and 1.6 to 3.6 V for the LCO cathode. For the CC-CV charge process, the cut-off conditions were defined as either the current reaching 1/10 of the current under the CC process or reaching the maximum allowed time under the specific rate (such as 1 h for 1 C). All groups were tested at least twice with the same trend.

Theoretical Modeling

Simulations of the NMC811 cathode were conducted using the Newman P2D model implemented in COMSOL Multiphysics 6.3. A summary of the parameters used for this study is given in Supplementary Table 2 and Supplementary Fig. 24, and the governing equations have been described in previous work[40]. The electrolyte fractions were determined from the mass loading of the sample and measured thickness of the electrodes, and a significant porosity in the samples was determined (25%). Several model parameters were chosen empirically to match trends in experimental data, notably the ionic conductivity in the electrolyte phase and the tortuosity of each layer in the three-layer electrode designs. The ionic conductivity in the catholyte was assumed to be 0.1 S/m, which is less than that of the experimental measurements of the SE. This assumption justified in that the solid electrolyte structure is altered during the processing of the catholyte. The tortuosity τ^2 values were approximated by a Bruggeman-type correlation for different electrolyte fractions (ϵ_e) in the layered structures, $\tau^2 = \epsilon_e^{-2.8}$; this is similar to that used in Stavola et al.[21]. (which reported a Bruggeman correlation of $\tau^2 = \epsilon_e^{-2.7}$). This correlation was used to calculate tortuosity for the low-electrolyte fraction layer C ($\epsilon_e = 0.26$, $\tau^2 = 42$) and "normal" electrolyte fraction layer B ($\epsilon_e = 0.35$, $\tau^2 = 19$). However, the "high" electrolyte faction layer A with this correlation ($\epsilon_e = 0.44$, $\tau^2 = 10$) did not produce a substantial change in predicted capacity expected for the three-layer electrode model, as compared to experiments; to account for this, it was assumed that the tortuosity was lower, with a value of $\tau^2 = 5$. This may account for different local structure of the electrolyte at higher electrolyte fractions, deviating from the low electrolyte fraction values.

Simulations were conducted to evaluate the predicted voltage response and capacity, local average intercalation fraction, and particle surface intercalation fraction for different electrode designs (conventional, three-layer, and reversed three-layer), various charge rates, and mass loadings. Simulated voltage profiles for varying mass-loadings and varying layer design are shown in Supplementary Figs. 15 and 25, respectively, and can be compared to Figs. 3a–c and 4d–f, respectively. It should be noted that these models are used to elucidate trends in the experimental data and do not necessarily represent detailed predictive models. The COMSOL input files for all modeling data presented in this work are provided in the Source Data file.

Data availability

The data generated in this study are provided in the Source Data file. Source data are provided with this paper.

References

1. Randau, S. et al. Benchmarking the performance of all-solid-state lithium batteries. *Nat. Energy* **5**, 259–270 (2020).
2. Heubner, C. et al. From lithium-metal toward anode-free solid-state batteries: current developments, issues, and challenges. *Adv. Funct. Mater.* **31**, 2106608 (2021).
3. Bielefeld, A., Weber, D. A. & Janek, J. Microstructural modeling of composite cathodes for all-solid-state batteries. *J. Phys. Chem. C.* **123**, 1626–1634 (2018).
4. Wang, J. et al. High-areal-capacity thick cathode with vertically-aligned micro-channels for advanced lithium ion batteries. *Energy Storage Mater.* **39**, 287–293 (2021).
5. Yang, X., Doyle-Davis, K., Gao, X. & Sun, X. Recent progress and perspectives on designing high-performance thick electrodes for all-solid-state lithium batteries. *ETransportation* **11**, 100152 (2022).
6. Vargas-Barbosa, N. M. & Roling, B. Dynamic ion correlations in solid and liquid electrolytes: how do they affect charge and mass transport?. *ChemElectroChem* **7**, 367–385 (2020).
7. Shkrob, I. A., Okasinski, J. S., Rodrigues, M.-T. F. & Abraham, D. P. Electrochemical modeling and experimental verification of lithiation gradients in oxide cathodes of lithium-ion cells. *J. Electrochem. Soc.* **169**, 040503 (2022).
8. Singh, M., Kaiser, J. & Hahn, H. Thick electrodes for high energy lithium ion batteries. *J. Electrochem. Soc.* **162**, A1196 (2015).
9. Li, Y. et al. A lithium superionic conductor for millimeter-thick battery electrode. *Science* **381**, 50–53 (2023).
10. Adeli, P. et al. Boosting solid-state diffusivity and conductivity in lithium superionic argyrodites by halide substitution. *Angew. Chem. Int. Ed.* **58**, 8681–8686 (2019).

11. Zhou, L., Assoud, A., Zhang, Q., Wu, X. & Nazar, L. F. New family of argyrodite thioantimonate lithium superionic conductors. *J. Am. Chem. Soc.* **141**, 19002–19013 (2019).
12. Wu, D., Chen, L., Li, H. & Wu, F. Solid-state lithium batteries-from fundamental research to industrial progress. *Prog. Mater. Sci.* **139**, 101182 (2023).
13. Janek, J. & Zeier, W. G. Challenges in speeding up solid-state battery development. *Nat. Energy* **8**, 230–240 (2023).
14. Ye, L. & Li, X. A dynamic stability design strategy for lithium metal solid state batteries. *Nature* **593**, 218–222 (2021).
15. Yan, W. et al. Hard-carbon-stabilized Li–Si anodes for high-performance all-solid-state Li-ion batteries. *Nat. Energy* **8**, 800–813 (2023).
16. Ohno, S., Rosenbach, C., Dewald, G. F., Janek, J. & Zeier, W. G. Linking solid electrolyte degradation to charge carrier transport in the thiophosphate-based composite cathode toward solid-state lithium-sulfur batteries. *Adv. Funct. Mater.* **31**, 2010620 (2021).
17. Bielefeld, A., Weber, D. A., Rueß, R., Glavas, V. & Janek, J. Influence of lithium ion kinetics, particle morphology and voids on the electrochemical performance of composite cathodes for all-solid-state batteries. *J. Electrochem. Soc.* **169**, 020539 (2022).
18. Minnmann, P., Quillman, L., Burkhardt, S., Richter, F. H. & Janek, J. Editors' choice—quantifying the impact of charge transport bottlenecks in composite cathodes of all-solid-state batteries. *J. Electrochem. Soc.* **168**, 040537 (2021).
19. Wang, Y. & Li, X. Fast kinetics design for solid-state battery device. *Adv. Mater.* **36**, 2309306 (2024).
20. Davis, A. L. et al. Rate limitations in composite solid-state battery electrodes: revealing heterogeneity with operando microscopy. *ACS Energy Lett.* **6**, 2993–3003 (2021).
21. Stavola, A. M. et al. Lithiation gradients and tortuosity factors in thick NMC111-argyrodite solid-state cathodes. *ACS Energy Lett.* **8**, 1273–1280 (2023).
22. Cao, D., Zhang, Y., Ji, T. & Zhu, H. In operando neutron imaging characterizations of all-solid-state batteries. *MRS Bull.* **48**, 1257–1268 (2023).
23. Ziesche, R. F., Kardjilov, N., Kockelmann, W., Brett, D. J. & Shearing, P. R. Neutron imaging of lithium batteries. *Joule* **6**, 35–52 (2022).
24. Wei, X., Wang, X., An, Q., Han, C. & Mai, L. Operando X-ray diffraction characterization for understanding the intrinsic electrochemical mechanism in rechargeable battery materials. *Small Methods* **1**, 1700083 (2017).
25. Ghigna, P. & Quartarone, E. Operando x-ray absorption spectroscopy on battery materials: a review of recent developments. *J. Phys. Energy* **3**, 032006 (2021).
26. Cao, D. et al. Li dynamics in mixed ionic-electronic conducting interlayer of all-solid-state Li-metal batteries. *Nano Lett.* **24**, 1544–1552 (2024).
27. Cao, D. et al. Nondestructively visualizing and understanding the mechano-electro-chemical origins of "soft short" and "creeping" in all-solid-state batteries. *Adv. Funct. Mater.* **33**, 2307998 (2023).
28. Bradbury, R. et al. Visualizing reaction fronts and transport limitations in solid-state Li–S batteries via operando neutron imaging. *Adv. Energy Mater.* **13**, 2203426 (2023).
29. Bradbury, R. et al. Visualizing lithium ion transport in solid-state Li–S batteries using 6Li contrast enhanced neutron imaging. *Adv. Funct. Mater.* **33**, 2302619 (2023).
30. Lodding, A., Mundy, J. & Ott, A. Isotope inter-diffusion and self-diffusion in solid lithium metal. *Phys. Status Solidi* **38**, 559–569 (1970).
31. Xiao, Y. et al. Understanding interface stability in solid-state batteries. *Nat. Rev. Mater.* **5**, 105–126 (2020).
32. Banerjee, A., Wang, X., Fang, C., Wu, E. A. & Meng, Y. S. Interfaces and interphases in all-solid-state batteries with inorganic solid electrolytes. *Chem. Rev.* **120**, 6878–6933 (2020).
33. Tan, D. H. S. et al. Elucidating reversible electrochemical redox of Li6PS5Cl solid electrolyte. *ACS Energy Lett.* **4**, 2418–2427 (2019).
34. Kim, J. et al. Electrochemical profiling method for diagnosis of inhomogeneous reactions in lithium-ion batteries. *Cell Rep. Phys. Sci.* **4**, 101331 (2023).
35. Noh, H.-J., Youn, S., Yoon, C. S. & Sun, Y.-K. Comparison of the structural and electrochemical properties of layered Li [NixCoyMnz] O2 (x= 1/3, 0.5, 0.6, 0.7, 0.8 and 0.85) cathode material for lithium-ion batteries. *J. Power Sources* **233**, 121–130 (2013).
36. Chen, H. et al. Tortuosity effects in lithium-metal host anodes. *Joule* **4**, 938–952 (2020).
37. Song, K., Zhang, C., Hu, N., Wu, X. & Zhang, L. High performance thick cathodes enabled by gradient porosity. *Electrochim. Acta* **377**, 138105 (2021).
38. Chouchane, M., Yao, W., Cronk, A., Zhang, M. & Meng, Y. S. Improved rate capability for dry thick electrodes through finite elements method and machine learning coupling. *ACS Energy Lett.* **9**, 1480–1486 (2024).
39. Shodiev, A. et al. Deconvoluting the benefits of porosity distribution in layered electrodes on the electrochemical performance of Li-ion batteries. *Energy Storage Mater.* **47**, 462–471 (2022).
40. Mijailovic, A. S. et al. Analytical and numerical analysis of lithium plating onset in single and bilayer graphite electrodes during fast charging. *J. Electrochem. Soc.* **169**, 060529 (2022).
41. Cao, D. et al. Enhancing lithium stripping efficiency in anode-free solid-state batteries through self-regulated internal pressure. *Nano Lett.* **23**, 9392–9398 (2023).
42. Cao, D. et al. Unveiling the mechanical and electrochemical evolution of nanosilicon composite anodes in sulfide-based all-solid-state batteries. *Adv. Energy Mater.* **13**, 2203969 (2023).

Acknowledgements

This research used resources at the High Flux Isotope Reactor, a DOE Office of Science User Facility operated by the Oak Ridge National Laboratory. H.Z. acknowledges the primary support of the US Department of Energy (DOE), Office of Science, Office of Basic Energy Sciences under award number DESC0024528. The authors would like to acknowledge support from the US Department of Energy (DOE) Bioenergy Technologies Office (BETO) Projects under contract with UT-Battelle LLC. This manuscript was partially authored by UT-Battelle LLC under contract DE-AC05-00OR22725 with DOE. The US government retains and the publisher, by accepting the article for publication, acknowledges that the US government retains a nonexclusive, paid-up, irrevocable, worldwide license to publish or reproduce the published form of this manuscript, or allow others to do so, for US government purposes. DOE will provide public access to these results of federally sponsored research in accordance with the DOE Public Access Plan (http://energy.gov/downloads/doe-public-access-plan).

Author contributions

H.Z. conceived and supervised this study. Y.Z., J.T. and T.J. conducted the operando neutron imaging experiment; A.M. and B.S. conducted the simulation part. J.B., Y.Z., J.T., and T.J. processed the operando neutron imaging data; T.J., J.B., Y.Z., and J.T. analyzed the operando neutron imaging data; T.J. performed electrochemical experiments. T.J. prepared the initial draft of the manuscript, H.Z. provided modifications and critical revisions. A.M., J.T., J.W., J.B., Y.Z., Y.T., X.Z., and B.S. checked the manuscript; Y.T., X.Z., and O.O. contributed to the second-round revision and performed detailed language editing. All authors have read and agreed to the published version of the manuscript.

Competing interests

The authors declare no competing interests.

Additional information

Supplementary information The online version contains supplementary material available at https://doi.org/10.1038/s41467-025-62518-y.

Correspondence and requests for materials should be addressed to Hongli Zhu.

Peer review information *Nature Communications* thanks Tongchao Liu, Wei Kong Pang, and the other, anonymous, reviewer for their contribution to the peer review of this work. A peer review file is available.